Resonant soft x-ray and extreme ultraviolet magnetic scattering in nanostructured magnetic materials: fundamentals and directions

Jeffrey B. Kortright
Lawrence Berkeley National Laboratory
1 Cyclotron Road, Berkeley, CA 94720
JBKortright@lbl.gov

Theoretical and practical aspects of resonant magnetic and charge scattering in the soft x-ray and extreme ultraviolet spectral range are reviewed. Intensity-only measurements are considered because they are more efficient than polarization-resolving measurements. Two very different approaches are discussed and compared; transmission small-angle scattering described by a simple kinematical scattering model and specular reflection described by more complex yet standard magneto-optical formalisms. In both cases the scattered intensity is seen to contain distinct terms resulting from pure-charge scattering, pure-magnetic scattering, and charge-magnetic cross-terms, and emphasis is placed on distinguishing these contributions via their energy spectra and its dependence on incident polarization. Combined with measurements vs. scattering vector q, both approaches provide significant capability to resolve magnetic and chemical structure down to nanometer length scales. The role of and need for modeling to obtain reliable information from data is discussed, as are current directions and opportunities.

PACS: 75.25.-j; 75.70.-I; 75.75.-c; 78.20.Ls; 78.70.Ck

Introduction

The discovery of strong resonant magnetic terms in the atomic scattering factor expansion [1,2] has prompted a great deal of research using x-ray scattering to study magnetic materials that continues to this day. Dipole-allowed transitions to empty, spin-polarized 3*d* and 4*f* resonant intermediate states of magnetic transition metal (TM) and rare-earth (RE) elements originate from spin-orbit split 2*p* and 3*d* core levels, respectively, whose energies $h\nu$ of roughly 400 – 2000 eV (corresponding to wavelength λ = 3 – 0.6 nm) fall within the soft x-ray spectral range typically served by grating monochromators. Transitions to the same 3*d* and 4*f* resonant intermediate states originate from the 3*p* and 4*d* core levels, respectively, with 40 < $h\nu$ < 200 eV (30 nm < λ < 6 nm) in the extreme ultraviolet (EUV) spectral range. Large element-specific magneto-optical (MO) effects at these resonances facilitate their application to study the spatial distribution of magnetization via angle-resolved scattering. Using radiation from synchrotron and emerging free electron laser & lab-based higher harmonic generation sources [3,4], these element-specific MO effects bring significant new experimental opportunities. Following introductory comments, this paper briefly reviews some practical theoretical and experimental considerations of intensity-only resonant soft x-ray & EUV magnetic scattering in the context of recent applications, and comments on current and future directions for extended application of these approaches.

While resonant magnetic scattering mechanisms are essentially the same across all spectral regions, several practical aspects distinguish their application in the soft x-ray range [5]. One is that long soft x-ray wavelengths limit spatial resolution and usually, but not always, position crystalline Bragg peaks beyond the accessible range of scattering vector $\bar{q}$. Low-*q* techniques such as small-angle scattering and specular reflectivity are thus well-suited for soft x-ray studies. Another is that strong soft x-ray absorption significantly limits penetration into samples and requires in-vacuum measurement. This strong absorption also means that the imaginary part of relevant scattering factors or optical constants must be included in calculations of scattering effects, while in the hard x-ray range absorptive terms are often small and ignored. These attributes make soft x-ray resonant scattering well-suited to study magnetic behavior in nanostructured materials, thin films and layered heterostructures, and near-surface regions of bulk magnetic and other correlated electron systems.

The term scattering encompasses many different processes and types of measurements and can mean rather different things to different researchers. Here we take scattering to mean resonant elastic scattering measured as a function of scattering angle 2θ, x-ray energy $h\nu$, incident and possibly scattered x-ray polarization, applied magnetic field *H*, temperature, and possibly other parameters. Angle-resolved scattering is practiced in several different scattering geometries, all of which are relevant to resonant magnetic scattering. In all cases structural correlations are probed along the scattering vector $\bar{q} = \bar{k}_f -$

$\bar{k}_o$ where $\bar{k}_o$ and $\bar{k}_f$ are the wave vectors of the incident and scattered wave fields as in Figure 1. Below we consider the cases of scattering in transmission from thin films and specular reflectivity as in Figure 2(a) and (b).

Finally, thinking in terms of resonant *magnetic* scattering can be misleading because resonant (and non-resonant) *charge* scattering always accompanies the magnetic part. Thus we must consider the interplay between charge and magnetic scattering amplitudes when planning and interpreting experiments. This interplay is both ubiquitous and strongly dependent on specific samples and different parameters as detailed below. The combined sensitivity to chemical and magnetic properties is significant as the two are usually highly correlated in space and it is frequently the imperfections in these correlations that are of interest in specific material systems. The ultimate utility of resonant soft x-ray magnetic scattering will thus depend on how well we can measure and model often-subtle details in terms of mixed chemical and magnetic heterogeneity.

Theoretical and practical considerations

The resonant atomic scattering factor $f(h\nu)$ expansion [1] provides the fundamental description of the distinct charge and magnetic x-ray scattering amplitudes as

$$f = \left(\hat{e}_f^* \cdot \hat{e}_o\right) f_c - i\left(\hat{e}_f^* \times \hat{e}_o\right) \cdot \hat{m} f_{m1} + \left(\hat{e}_f^* \cdot \hat{m}\right)\left(\hat{e}_o \cdot \hat{m}\right) f_{m2} + \cdots. \quad (1)$$

Here $\hat{e}_o$ and $\hat{e}_f^*$ are unit polarization vectors of the incident and scattered wavevectors, respectively, and $\hat{m}$ is a unit vector along the axis of local magnetization of the scattering atom. The f_c, f_{m1}, and f_{m2} terms describe distinct linear combinations of matrix elements between initial and resonant intermediate states resolved according to spherical harmonics Y_{LM} and hence angular momentum increment of the transitions involved. Only electric dipole (*EL* with *L* = 1, ΔM = -1, 0, 1) terms are retained in (1). We group the non-resonant charge term (approximately the atomic number *Z*) together with the resonant charge term in f_c as they have the same polarization dependence. Distinct polarization dependencies describe the different interactions between the radiation field and the charge, f_c, and 1st & 2nd order magnetic terms, f_{m1} & f_{m2}, respectively. These polarization dependencies reveal that f_{m1} manifests as well-known magnetic circular dichroism effects while f_{m2} manifests as magnetic linear dichroism.

The polarization of incident and scattered radiation fields and the direction of local atomic moments are key parameters in resonant magnetic scattering. Transverse polarization can be described alternatively by orthogonal linear ($\hat{e}_s$ and $\hat{e}_p$) or opposite helicity circular ($\hat{e}_+$ and $\hat{e}_-$) basis vectors [6]. Linear and circular polarization basis vectors are related by

$$\hat{e}_s = \begin{pmatrix}1\\0\end{pmatrix}, \hat{e}_p = \begin{pmatrix}0\\1\end{pmatrix}, \hat{e}_+ = \frac{\hat{e}_s + i\hat{e}_p}{2} = \frac{1}{\sqrt{2}}\begin{pmatrix}1\\i\end{pmatrix}, \hat{e}_- = \frac{\hat{e}_s - i\hat{e}_p}{2} = \frac{1}{\sqrt{2}}\begin{pmatrix}1\\-i\end{pmatrix}. \quad (2)$$

As in Figure 1 the atomic moment $\hat{m}$ can have longitudinal, transverse, and polar projections (m_l, m_t, m_p, respectively) relative to the scattering plane and the Cartesian axes. The total scattering angle is 2θ. Considering the polarization dependence of just the first two terms of (1) and using a linear (*s*- and *p*-polarization) basis yields an expression for the *s*- and *p*-polarized components of the scattered radiation field $\bar{E}^f$ in terms of the incident field $\bar{E}^o$ [7], namely

$$\begin{pmatrix}E_s^f\\E_p^f\end{pmatrix} = \left[f_c\begin{pmatrix}1 & 0\\0 & \cos 2\theta\end{pmatrix} - if_{m1}\begin{pmatrix}0 & m_p\sin\theta + m_l\cos\theta\\m_p\sin\theta - m_l\cos\theta & m_t\sin 2\theta\end{pmatrix}\right]\begin{pmatrix}E_s^o\\E_p^o\end{pmatrix}, \quad (3)$$

where the 2-by-2 matrices account for the scattering effects on the polarization components of the fields. Completely different polarization behavior is exhibited by the charge and 1st order magnetic term. Charge scattering preserves polarization aside from the suppression in the *p* channel that yields the Brewster angle at $2\theta \cong 90°$. The off-diagonal elements associated with f_{m1} yield *s* to *p* scattering (and vice versa) due to both m_p and m_l components, *p* to *p* scattering from the m_t component, and no *s* to *s* scattering.

All Faraday and Kerr magneto-optical effects familiar in the near-visible spectral region are embodied in (1) – (3) [8, 9]. This leads naturally to questions of the value and feasibility of measurements in which the polarization state of scattered x-rays is measured directly, as opposed to intensity-only measurements that do not resolve polarization. Linear polarizers required for polarization analysis result from charge scattering, typically specular reflectivity, as described by the 1st term of (3). At the Brewster angle the ratio of *s*- to *p*-polarized scattered intensity, $\left|E_s^f\right|^2/\left|E_p^f\right|^2$, can be quite high, although absolute reflected intensities from x-ray mirrors are quite low and generally decrease with λ. Multilayer interference films increase reflectivity [10, 11, 12,13] and enable polarization analysis, although these devices tend to be chromatic and also suffer from reduced efficiency as λ decreases. Phase retarding optics based on multilayers, used with linear polarizers to resolve circular from unpolarized radiation or to convert linear to elliptical polarization, are even more challenging in the soft x-ray range due to low efficiency and chromaticity [10, 14, 15]. Circular polarizers utilizing magnetic circular dichroism have been demonstrated [16, 17, 18] and are also very chromatic. Thus, while polarization measurements of scattered beams are possible in favorable cases, they are inefficient and not generally feasible because of limited performance of required optical elements. This places added emphasis on understanding intensity-only measurements of magnetic scattering effects in the soft x-ray spectral range

[19], which we consider here. Of course, polarization-resolved measurements can be of considerable value when they are made.

The resonant energy dependence of the f_c, f_{m1}, and f_{m2} terms are distinct yet related and their absorption spectroscopy is a rich subject in itself [20, 21]. While we do not review these spectroscopic aspects in detail here, it is important to realize that they determine the $h\nu$-dependence of resonant scattered intensities in useful ways as demonstrated below. The real and imaginary parts of $f_c = f_{c,1} + if_{c,2}$ and $f_{m1} = f_{m1,1} + if_{m1,2}$ for a metallic Fe film [9] and Co in a Co/Pt multilayer [22] are shown below in Figures 7(b) and (c) across their L_3 and L_2 edges. The real and imaginary parts of both charge and magnetic terms are related via the Kramers-Kronig dispersion relation. The strong L_3 and L_2 resonance lines are characteristic of 3*d* transition elements, and for $f_{c,2}$ their sum is proportional to the number of *d* holes. The characteristic dipolar spectral shape of $f_{m1,2}$ can be analyzed in terms of sum rules to obtain the ratio of spin to orbital moments [23, 24, 20]. Compared to relatively featureless (band-like) resonant lines of itinerant magnetic metals, absorption spectra of 3*d* TM elements in oxides and other correlated systems are often richer as crystal field effects split spectral lines into distinct multiplets providing information on filling and symmetry of the 3*d* manifold [21]. The spectral dependence of $f_{m2,2}$ tends to resemble the derivative of $f_{m1,2}$ and is quite weak compared to it [9, 25]; this term has not generally been considered explicitly in soft x-ray resonant scattering experiments to date. In principle the 3*d* transition metal M_3 and M_2 lines at 3*p* core levels contain similar information to the L_3 and L_2 lines at the 2*p* core levels and have been used in magnetic spectroscopy and scattering [26, 27, 28]. The spin-orbit coupling in the 3*p* levels is small compared to that in the 2*p* levels, so that well-separated L_3 and L_2 lines show significant overlap for the M_3 and M_2 lines, and indeed the lines for adjacent elements show some spectral overlap. For magnetic rare earth elements the M_5 and M_4 lines originating from the 3*d* core levels are even stronger than the L_3 and L_2 lines for the 3*d* transition series and exhibit larger spin-orbit splitting. The author is unaware of resonant magnetic spectroscopy or scattering at the rare earth N_5 and N_4 lines sampling the 4*f* resonant intermediate states from the 4*d* core levels.

Scattering can be measured in any of the common scattering geometries illustrated in Figure 2. The geometry chosen should optimize the coupling of $\bar{q}$ to the magnetic and charge structure of interest, consistent with sample and other constraints. Depth-dependent structure in films is best studied using specular reflectivity (Fig. 2a) that varies $\bar{q}$ along the sample normal [29, 30], while in-plane thin film structure is well-studied in symmetric transmission geometry (Fig. 2b) if transmission samples are feasible [22, 31, 32]. Off-specular reflectance (Fig. 2c) and grazing incidence (Fig. 2d) geometries also provide an in-plane $\bar{q}$ component to study in-plane structure that is most commonly thought of as

originating from interfacial contrast [33, 34], although magnetic heterogeneity internal to films also yields measurable scattering in these geometries [35]. If variable applied magnetic fields of even modest strength are desired, the incorporation of suitable magnets in an ultrahigh vacuum chamber generally limits the scattering angles 2θ and geometries accessible. Such instrument-related considerations imply that no single scattering chamber is likely to optimize the angle- and field-dependent requirements of all measurements of interest.

The spatial resolution of scattering in real space is inversely proportional to the q-range measured in reciprocal space, and since $|\bar{q}| = 4\pi sin\theta/\lambda$, we can expect to resolve smaller structure at the TM $L_{3,2}$ and RE $M_{5,4}$ edges than at the TM $M_{3,2}$ and RE $N_{5,4}$ edges. However, like in the visible regime [36], calculations [37, 38] and measurements [37, 39] confirm that soft x-ray reflectance measurements, *e.g.*, are sensitive to magnetic layers much thinner than could be resolved according to this Fourier limit. Element-specificity through spectroscopy brings an added avenue to spatial resolution [40], which thus can be usefully considered to arise from different origins.

The sensitivity to different magnetic projections evolves systematically with scattering angle according to (1) and (3) as in Figure 3. In this figure solid lines give the θ dependence of f_{m1} amplitudes or the Re$[f_c^* f_{m1}]$ intensity cross term, while dashed lines correspond to the $f_{m1}^* f_{m1}$ intensity term. Dominant sensitivity to longitudinal moments at low angles is evident, as is dominant sensitivity to polar moments in the high angle limit. Transverse moment sensitivity is maximum at θ = 45°, where polarization dependent sensitivity to m_l and m_p also exists. The f_{m1} amplitudes change sign as each projected $\hat{m}$ component changes sign, and how this manifests in the scattered intensity will depend on whether the f_{m1} amplitudes contribute as pure-magnetic or charge-magnetic terms, on 2θ, and on the specific x-ray polarization under consideration. Measured scattered intensities will generally contain different magnetic contributions involving different moment projections as in (3) that can lead to many terms in model expressions. Examples discussed in detail below involve limited moment orientations for simplicity, although many studies cited involve more complicated distributions of moments.

Magnetic scattering in the kinematical limit

Distinct charge and magnetic terms in the scattering amplitude lead to distinct terms in the scattered intensity. Some useful generalizations regarding the interplay between $\hat{e}_o$ and scattering intensities result from examining the dominant sensitivity to longitudinal magnetization (m_l) at small 2θ. In the limit that $\theta \to 0$ equation (3) reduces to

$$\begin{pmatrix} E_s^f \\ E_p^f \end{pmatrix} = \begin{pmatrix} f_c & -im_l f_{m1} \\ im_l f_{m1} & f_c \end{pmatrix} \begin{pmatrix} E_s^o \\ E_p^o \end{pmatrix}. \quad (4)$$

Because of the large resonant magnetic circular dichroism associated with the f_{m1} term, it was natural for early soft x-ray magnetic scattering experiments [41, 42, 43, 44, 45, 46] to utilize circular incident polarization to obtain sensitivity to magnetic structure. Assuming opposite helicity circular polarization as incident radiation yields

$$I_{\pm} = f_c^* f_c s_{cc}(q) \pm 2\mathrm{Re}[m_l f_c^* f_{m1}] s_{cm}(q) + m_l^2 f_{m1}^* f_{m1} s_{mm}(q) \quad (5)$$

containing pure-charge and pure-magnetic contributions plus the charge-magnetic cross term that reverses sign with helicity. Here we have introduced partial structure factors $s_{ij}(q)$ containing the spatial frequency dependence of the indicated pair correlations. The circular difference

$$I_+ - I_- = 4\mathrm{Re}[m_l f_c^* f_{m1}] s_{cm}(q) \quad (6)$$

leaves only the charge-magnetic cross term [47, 22]. The circular sum

$$I_+ + I_- = 2(f_c^* f_c s_{cc}(q) + m_l^2 f_{m1}^* f_{m1} s_{mm}(q)) \quad (7)$$

yields just pure-charge and pure-magnetic terms [22,48]. Considering linear incident polarization yields

$$I_{lin} = f_c^* f_c s_{cc}(q) + m_l^2 f_{m1}^* f_{m1} s_{mm}(q) = (I_+ + I_-)/2\,, \quad (8)$$

consistent with the understanding that $\hat{e}_s$ and $\hat{e}_p$ are a coherent superposition of $\hat{e}_+$ and $\hat{e}_-$, and *vice versa*. Thus, for small 2θ, linear incident polarization yields pure-charge plus pure-magnetic intensity terms and is equivalent to the intensity obtained by summing opposite helicity circular incident polarization. Whether linear or circular polarization is more appropriate for a given study depends on the conditions specific to that study, including whether or not one is interested in resolving the q-dependence of the different partial structure factors. With judicious parameter choice, partial or complete separation of different contributions of specific interest may be possible. With this goal in mind, the scattering asymmetry defined as $(I_+ - I_-)/(I_+ + I_-)$ contains a complex combination of all possible terms and so may be less useful in isolating different contributions of interest.

This simple kinematical, or single scattering, model thus makes clear and specific predictions about magnetic scattering and its interactions with charge scattering and polarization. In the course of studying several systems these predictions have tested as briefly outlined below.

Testing the kinematical theory in small-angle scattering geometry

Thin films having pronounced perpendicular magnetic anisotropy (PMA) are currently of interest in the quest for higher density magnetic storage media [49]. Co/Pt multilayer films are prototypical high PMA films and, depending on their microstructure, may or may not form submicron domains to lower magnetostatic energy at remenance. Such films have provided numerous opportunities to test the theoretical model above. Because the stripe domains in PMA films have moments predominantly normal to the film plane (arrows in Fig. 2b) and relatively large size, the transmission scattering geometry is ideally suited to study such structures that closely approximate expressions for the low angle, longitudinal limit developed above.

Transmission scattering vs. in-plane q at the Co L_3 edge from Co/Pt at the coercive and saturation applied fields (H_C and H_S, respectively) are plotted as open symbols in Figure 4. These data were measured using linear (s) incident polarization. At the coercive field (H_C = 0.1 T) a strong low-q peak corresponds to a spatial wavelength $2\pi/q$ = 150 nm. This peak disappears at saturation, confirming that it results from the magnetic domain structure, leaving a weaker peak at higher q that appears to be non-magnetic in origin. Magnetic microscopy confirms that the low-q peak results from magnetic domain scattering. Atomic force microscopy of the surface morphology confirms that the higher q peak corresponds to the surface height power spectrum characteristic of the polycrystalline grain size in these films [22]. The q dependence of this scattering is thus consistent with relatively distinct and sharp pure-magnetic and pure-charge correlation lengths, represented by the low-q peak at H_C and the high-q peak, respectively. The position of the pure-magnetic peak gives a model-independent measure of the ensemble-average, up-down stripe domain period.

The field dependence of measured intensity at the low-q peak through a major hysteresis loop is shown in Figure 5. Weak scattering at saturation persists until the first reverse domains emerge at the nucleation field H_N. The scattering rises rapidly to a maximum at the coercive field H_C where the widths and number of up and down stripe domains are roughly equal, and returns to the same low value as the last domains disappear. The scattering hysteresis loop gives an ensemble-average, microscopic view of how magnetization heterogeneity evolves at a specific spatial frequency. This is distinctly different from, and yet consistent with, traditional magnetometry that senses the macroscopic average of the magnetization through the reversal cycle. The symmetry of the scattering hysteresis loop is consistent with the pure-magnetic origin of this scattering, whereby $f_{m1}^* f_{m1}$ always adds to a weak $f_c^* f_c$ background with equal intensity on both branches of the major hysteresis loop.

The energy dependence of the scattering provides yet another test of the kinematical model predictions. Figure 6 shows such scattering spectra measured at both H_S and H_C at q values corresponding to the magnetic and the intergranular peaks in Fig. 4. According to (8) these spectra should be fit by linear combinations of pure-charge and pure-magnetic terms. As developed in Ref. [22], the fits (lines) to these data are well-described by combinations of pure-charge and magnetic contributions using the measured f_{m1} and f_c spectra for Co shown in Fig. 7(b) and (c). In particular, the scattering spectrum in Fig. 6a at the low-q magnetic peak and H_C is fit using only $f_{m1}^* f_{m1}$, and at 1 T with a flat intensity scaled by the sample's transmission spectrum. The spectrum measured at the high-q peak at H_S in Fig. 4b is well modeled as a pure-charge spectrum in which both resonant Co and non-resonant Pt charge scattering factors contribute. At H_C this high-q peak is modeled by the same charge spectrum plus a small amount of resonant Co $f_{m1}^* f_{m1}$.

All of the resonant scattering measured using linear polarization from these Co/Pt samples is consistent with eqn. (8) that the intensity is described as a combination of pure-charge and pure-magnetic scattering. The prediction that intensity measured using linear polarization is equivalent to the average of intensities measured using opposite helicity circular polarization was quantitatively confirmed in a separate study of scattering from dense assemblies of super-paramagnetic Co nanoparticles [48]. This study also considered a random 3-dimensional distribution of interparticle moment orientations and developed a simple model to determine if data indicate thatinterparticle magnetic correlations are significant. The strong magnetic scattering from the Co/Pt multilayer system, and related films exhibiting strong PMA have been used to study magnetic domain memory [50, 51, 52], competing interactions within magnetic multilayer films [53, 54], holographic reconstruction of domain images [55], phase-retrieval imaging [56], and most recently as test objects in XFEL measurements [57,18].

Specular reflectivity: x-ray magneto-optical Kerr intensity effects

Resonant soft x-ray specular reflectivity studies to obtain depth-resolved magnetization and chemical information extend near-visible magneto-optical Kerr effects to benefit from element-specificity and an extended q range. Formalisms developed for layered structures in the visible [8] are readily extended into the x-ray regime [9, 58]. As mentioned above, depth-resolving capabilities in the soft x-ray range can be considered to originate from both spectroscopic and q-resolved sensitivity, and are maximized by combining information from both approaches [30,40]. Compared to the kinematical model considered above, reflectivity studies of layered systems involve multiple reflections from internal interfaces and so are dynamical in nature [9, 59]. In such cases modeling is complicated by the compounding of strong resonant spectroscopic and structural phase contributions in reflected amplitudes.

Such considerations imply that careful modeling of data is more critical in reflectivity than in transmission studies.

Optical models describing soft x-ray Kerr effects are based on a second-rank tensor description of the dielectric constant or refractive index. The dielectric tensor is assumed to have the form

$$\varepsilon = n_c^2 \begin{pmatrix} 1 & iQm_p & -iQm_l \\ -iQm_p & 1 & iQm_t \\ iQm_l & -iQm_t & 1 \end{pmatrix} \tag{9}$$

where $n_c = (n_+ + n_-)/2$ gives the isotropic charge part of the refractive index and $Q = (n_+ - n_-)/n_c$ gives the MO response [9]. When mapped onto $\bar{k}_o$ and $\bar{k}_f$ and using matrices describing propagation through uniform media and continuity at interfaces, interference effects in complex magnetic structures are readily described via matrix multiplication [8]. The resulting Kerr matrix of reflection coefficients determines reflected from incident field components,

$$\begin{pmatrix} E_s^f \\ E_p^f \end{pmatrix} = \begin{pmatrix} r_{ss} & r_{ps} \\ r_{sp} & r_{pp} \end{pmatrix} \begin{pmatrix} E_s^o \\ E_p^o \end{pmatrix}, \tag{10}$$

from which polarization and intensity effects are evaluated.

Magneto-optical techniques in the visible spectral regime frequently measure polarization changes on reflection of incident linear polarization. While polarization-resolved soft x-ray MO measurements have been demonstrated [11, 60], they are non-trivial as discussed above and we consider here intensity-only signals. In particular, we look for relationships between the spectral response of reflected intensities using circular and linear polarization and their origin in pure-charge, pure-magnetic, and charge-magnetic terms as found above in the simple kinematical scattering model (eqns. (5) – (8)). Using the MO formalism just outlined, we evaluate reflection spectra under different conditions for a simple, hypothetical magnetic heterostructure comprised of an idealized Fe(3 nm)/Co(10 nm) magnetic bilayer on Si in which interfacial roughness and interdiffusion are absent and the surface is assumed to be free of oxidation and contamination. The charge and magnetic optical constants used to describe Fe [9] and Co [22] are in Figure 7(c) and (d), respectively.

First we consider the MO response in the small-angle, longitudinal $\hat{m}$ limit for this layered system as done above for transmission scattering. Reflectances R_+, R_-, R_s, and R_p are evaluated for the different circular and linear incident polarizations indicated as functions of both $h\nu$ and 2θ and for both parallel and antiparallel alignment of m_l in each layer. Figure 7(a) shows R_+ and R_- spectra at $2\theta = 20°$

for the case when m_l for each layer are aligned parallel as for ferromagnetic coupling. Figure 7(b) shows $R_+ - R_-$ spectra for both parallel and antiparallel alignment of the Fe and Co moments as indicated. The sign of the resonant $R_+ - R_-$ peaks at the Fe and Co resonant lines is the same when their moments are parallel, and opposite when antiparallel. This indicates that $R_+ - R_-$ is dominated by charge-magnetic interference scattering consistent with (6) and, more importantly, that such spectra provide a relatively direct measure of the sign of interfacial exchange coupling of longitudinal moments. This spectroscopic approach to determine the sign of exchange coupling has not yet been widely utilized in soft x-ray measurements [61], even though such energy spectra are straightforward to obtain. While relatively direct, this approach to determine the sign of exchange coupling would best be applied in conjunction with modeling to ensure that structural imperfections or interference features do not complicate interpretations [62, 63].

In looking for evidence of pure-charge plus pure-magnetic intensity terms using linear polarization, as in (7) and (8), we find that the pure-magnetic effects are observed in calculations where different polarization components are retained to give Kerr rotation, and are less observable in intensity measurements. The small size of the pure-magnetic contribution relative to the pure-charge contribution in reflection, compared to that observed in the transmission scattering example above, results from the relative size of the diagonal and off-diagonal terms in (9). The relevant resonant optical parameters $\delta_c,\ \delta_{m1} \ll 1$ and $\beta_c,\ \beta_{m1} \ll 1$ enter in the index of refraction as $n_c = 1 - \delta_c + i\beta_c \cong 1$, while $Q \cong -\delta_{m1} + i\beta_{cm1} \ll 1$. Thus in reflection the charge scattering is referenced to the vacuum value of 1, while the purely resonant magnetic contribution has no contrast with the nonmagnetic vacuum. In the kinematical theory developed above, only contrast internal to the sample is considered, yielding magnetic scattering of the same order as the charge scattering as in (4) – (8) and Figs. 4-6.

A notable exception to this predominance of pure-charge over pure-magnetic terms in linear intensity measurements are transverse MO effects, *i.e.*, changes in m_t, that act on *p*-polarization and are maximized as θ approaches the Brewster angle where charge scattering is most strongly suppressed. This is illustrated in Figure 8 for the model bilayer where $R_p(h\nu)$ is plotted for 2 cases; one with $m_t = 1$ for Fe and -1 for Co (red), and the other for $m_t = 0$ for both layers (blue). The ratio of intensities in these two cases is roughly 10^3 over the entire spectral range because of the large suppression of the charge scattering. R_p is quite small in both cases. When $m_t \neq 0$ R_p is independent of its sign, so that the enhancement in intensity above the $m_t = 0$ case goes like Q^2 and this scattering is pure-magnetic in origin. Away from $\theta = 45°$ charge scattering is stronger and charge-magnetic interference intensity can easily overshadow the pure-magnet contribution. While this transverse intensity effect is maximized for

p-polarization, it is also present for circular polarization that has partial *p*-character. Transverse MO effects have been used in a Sm-Co/Fe exchange spring couple to observe the transverse moment in the interfacial domain wall within the soft Fe layer resulting from its coherent rotation during reversal [64], and in other settings [65, 66, 26, 67, 68].

To summarize this very brief discussion of intensity-only resonant magnetic reflectivity effects, circular polarization is sensitive to longitudinal and polar and moments and $R_+ - R_-$ removes strong pure-charge and weak pure-magnetic contributions to isolate intensity with charge-magnetic character. Transverse moments show up most strongly using *p*-polarization and have pure-magnetic charge-magnetic contributions. Reflectivity with incident *p*-polarization is insensitive to m_l and m_p. However, circular polarization is sensitive to changes in m_t because it is composed of both *s*- and *p*-polarization components. Thus intensity-only measurements are sensitive all moment orientations provided suitable polarizations are used and careful analysis is made. Three-dimensional moment distributions vs. depth can be resolved with intensity-only intensity measurements with careful modeling [39] that benefit from a large 2θ range in which the weighting of different projections varies systematically.

As for the kinematical scattering model developed above, distinct $f_c^* f_c$, $f_{m1}^* f_{m1}$, and Re$[f_c^* f_{m1}]$ intensity contributions in reflection are evident through the symmetries they display with changes in $\hat{m}$ and $\hat{e}_o$. The kinematical model ignores polarization changes within the sample on scattering, while the MO formalism explicitly accounts for polarization changes as wave fields propagate and interfere within samples. This yields rich and complex resonant behavior containing much information that in turn requires careful modeling to extract.

Current directions and future opportunities

Considering the importance of magnetic materials that are structured at nanometer and greater length scales in both fundamental and applied settings, resonant soft x-ray scattering studies offer much potential to gain relevant, new insight. Several current directions and future opportunities and challenges are briefly mentioned here.

Resonant x-ray scattering is compatible with ultrafast studies using visible laser or other pump sources to probe ensuing magnetization (and charge) dynamics. Recent studies involve both specular reflectivity and transmission scattering modes [69, 18, 57, 61, 67, 68]. These early ultrafast studies are revealing new details regarding ultrafast spin dynamics that are yet to be fully understood. To date, reflectivity studies have focused primarily on element specific dynamics using resonant sensitivity and observed changes are usually assumed to be magnetic in origin. More information will be obtained from

such measurements by combining careful modeling of temporal, depth, and spectral dependence of resonant f_c and f_{m1} since both can exhibit dynamic responses. Furthermore, laser-pump x-ray probe studies to date have generally measured x-ray signals originating from the same sample volume that is photo-excited by the laser. Soft x-ray skin depths can be significantly greater than visible pump skin depths. This points both to the need for care in interpreting resonant magnetic scattering signals in general, and to new opportunities to study how energy flows out of the photo-excited region into deeper regions of samples.

We have emphasized here that the energy dependence of resonant magnetic scattering or reflectance can contain much information regarding the specific contributions to scattering and how they vary with q. Indeed in the domain scattering example, measured charge and magnetic scattering factors were used to fit the scattering spectra and further validate the kinematical scattering model. In this case care was taken to measure the relevant absorption spectra with a minimum of residual artifacts. However the availability of accurate resonant f_c and f_{m1} spectra to describe regions of interest in specific samples is not certain for different reasons. One is that accurate absorption spectra from buried regions of samples are not always available experimentally [9]. More fundamentally, one's goal may be to determine unknown spin-dependent electronic structure that exists only at buried interfaces between chemically dissimilar materials. In such cases, self-consistent modeling of both the $h\nu$- and q-dependence of measured reflectivity data, for example, would help to ensure that resulting f_c and $f_{m1}$and their spatial variation is as accurate as possible. Progress on such self-consistent modeling of the spatial and spectral variation of f_c and has recently been reported in studies of off-stoichiometric subsurface layers in $SrTiO_3$ crystals [70, 71]. Such modeling is effectively a form of generalized spectroscopic ellipsometry that benefits from large $R(q, h\nu)$ datasets readily available at synchrotron sources. Extensions to include f_{m1} spectral modeling should be straight-forward.

An implicit assumption above is that (spherically symmetric) E1 f_c and f_{m1}terms adequately describe the relevant scattering processes. While this may be true in some cases, others of current and future interest will involve added anisotropies beyond those considered here. Examples of such cases include magnetism in complex oxides, multiferroic systems, and heterostructures in which interfacial properties of interest may have different or even unknown local symmetries. In addition to the f_{m2} term describing magnetic linear dichroism, higher order electric and magnetic multipole terms describing other anisotropies will exist in specific cases [1, 72, 73, 74, 75, 76]. Added anisotropies will generally add terms and possibly dimensions to the dielectric tensor, and more amplitudes will yield more intensity contributions (both pure- and cross-terms) that may or may not be simply separable. Again, this complexity presents both analytical challenges and opportunities.

Conclusions

The sensitivity of resonant soft x-ray scattering to magnetic and charge structure suggests that its use will continue to grow. Considerations discussed here reveal a rich parameter-space in which resonant magnetic scattering can be beneficially applied to study a wide range of phenomena in magnetic systems. In addition to the polarization and magnetization dependence of distinct charge and magnetic contributions, element-specific spectroscopic differences and angular dependent sensitivity to the spatial distribution of scattering centers all provide distinct opportunities to gain new insights into specific questions of fundamental and applied interest. While the planning for and interpretation of experimental results requires careful attention, the availability of suitable instrumentation may also limit the growth in the application of these approaches.

Acknowledgements

This work, including measurements conducted at beamlines 8.0.1, 4.0.2, and 6.3.2 at the Advanced Light Source (LBNL), was supported by the U. S. Department of Energy, Office of Basic Energy Sciences, Division of Materials Science under Contract No. DE-AC02-05CH11231.

References

1. J. P. Hannon, G. T. Trammell, M. Blume, and D. Gibbs, Physical Review Letters **61**, 1245 (1988).
2. D. Gibbs, D. R. Harshman, E. D. Isaacs, D. B. McWhan, D. Mills, and C. Vettier, Physical Review Letters **61**, 1241 (1988).
3. A. Rundquist, C. G. Durfee, Z. H. Chang, C. Herne, S. Backus, M. M. Murnane, and H. C. Kapteyn, Science **280**, 1412 (1998).
4. R. Berlasso, C. Dallera, F. Borgatti, C. Vozzi, G. Sansone, S. Stagira, M. Nisoli, G. Ghiringhelli, P. Villoresi, L. Poletto, M. Pascolini, S. Nannarone, S. De Silvestri, and L. Braicovich, Physical Review B **73**, 115101 (2006).
5. The term soft x-ray is used broadly to encompass the EUV spectral range, unless otherwise specified.
6. D. Goodman, *Polarized Light* (Marcel Dekker, New York, 2003).
7. J. P. Hill, and D. F. McMorrow, Acta Crystallographica Section A **52**, 236 (1996).
8. J. Zak, E. R. Moog, C. Liu, and S. D. Bader, Physical Review B **43**, 6423 (1991).
9. J. B. Kortright, and S. K. Kim, Physical Review B **62**, 12216 (2000).
10. J. B. Kortright, and J. H. Underwood, Nuclear Instruments & Methods in Physics Research A **291**, 272 (1990).
11. J. B. Kortright, M. Rice, and R. Carr, Physical Review B **51**, 10240 (1995).
12. J. B. Kortright, M. Rice, and K. D. Franck, Review of Scientific Instruments **66**, 1567 (1995).
13. F. Schafers, H. C. Mertins, A. Gaupp, W. Gudat, M. Mertin, I. Packe, F. Schmolla, S. Di Fonzo, G. Soullie, W. Jark, R. Walker, X. Le Cann, R. Nyholm, and M. Eriksson, Applied Optics **38**, 4074 (1999).
14. J. B. Kortright, H. Kimura, V. Nikitin, K. Mayama, M. Yamamoto, and M. Yanagihara, Applied Physics Letters **60**, 2963 (1992).
15. M. A. MacDonald, F. Schafers, and A. Gaupp, Optics Express **17**, 23290 (2009).
16. J. B. Kortright, S. K. Kim, T. Warwick, and N. V. Smith, Applied Physics Letters **71**, 1446 (1997).
17. S. K. Kim, J. B. Kortright, and S. C. Shin, Applied Physics Letters **78**, 2742 (2001).
18. T. H. Wang, D. L. Zhu, B. Wu, C. Graves, S. Schaffert, T. Rander, L. Muller, B. Vodungbo, C. Baumier, D. P. Bernstein, B. Brauer, V. Cros, S. de Jong, R. Delaunay, A. Fognini, R. Kukreja, S. Lee, V. Lopez-Flores, J. Mohanty, B. Pfau, H. Popescu, M. Sacchi, A. B. Sardinha, F. Sirotti, P. Zeitoun, M. Messerschmidt, J. J. Turner, W. F. Schlotter, O. Hellwig, R. Mattana, N. Jaouen, F. Fortuna, Y. Acremann, C. Gutt, H. A. Durr, E. Beaurepaire, C. Boeglin, S. Eisebitt, G. Grubel, J. Luning, J. Stohr, and A. O. Scherz, Physical Review Letters **108**, 267403 (2012).

19. H. C. Mertins, S. Valencia, D. Abramsohn, A. Gaupp, W. Gudat, and P. M. Oppeneer, Physical Review B **69**, 064407 (2004).
20. J. Stohr, and H. C. Seigmanm, *Magnetism From Fundamentals to Nanoscale Dynamics* (Springer, Berlin, 2006).
21. F. deGroot, and A. Kotani, *Core Level Spectroscopy of Solids* (CRC Press, Boca Raton, 2008).
22. J. B. Kortright, S. K. Kim, G. P. Denbeaux, G. Zeltzer, K. Takano, and E. E. Fullerton, Physical Review B **64**, 092401 (2001).
23. C. T. Chen, Y. U. Idzerda, H. J. Lin, N. V. Smith, G. Meigs, E. Chaban, G. H. Ho, E. Pellegrin, and F. Sette, Physical Review Letters **75**, 152 (1995).
24. R. Nakajima, J. Stohr, and Y. U. Idzerda, Physical Review B **59**, 6421 (1999).
25. J. Kunes, and P. M. Oppeneer, Physical Review B **67**, 024431 (2003).
26. M. Hecker, P. M. Oppeneer, S. Valencia, H. C. Mertins, and C. M. Schneider, Journal of Electron Spectroscopy and Related Phenomena **144**, 881 (2005).
27. S. Valencia, A. Gaupp, W. Gudat, H. C. Mertins, P. M. Oppeneer, D. Abramsohn, and C. M. Schneider, New Journal of Physics **8**, 254 (2006).
28. J. Kunes, P. M. Oppeneer, S. Valencia, D. Abramsohn, H. C. Mertins, W. Gudat, M. Hecker, and C. M. Schneider, Journal of Magnetism and Magnetic Materials **272**, 2146 (2004).
29. J. M. Tonnerre, L. Seve, D. Raoux, G. Soullie, B. Rodmacq, and P. Wolfers, Physical Review Letters **75**, 740 (1995).
30. S. Roy, M. R. Fitzsimmons, S. Park, M. Dorn, O. Petracic, I. V. Roshchin, Z. P. Li, X. Batlle, R. Morales, A. Misra, X. Zhang, K. Chesnel, J. B. Kortright, S. K. Sinha, and I. K. Schuller, Physical Review Letters **95**, 047201 (2005).
31. E. E. Fullerton, O. Hellwig, Y. Ikeda, B. Lengsfield, K. Takano, and J. B. Kortright, Ieee Transactions on Magnetics **38**, 1693 (2002).
32. O. Hellwig, D. T. Margulies, B. Lengsfield, E. E. Fullerton, and J. B. Kortright, Applied Physics Letters **80**, 1234 (2002).
33. S. K. Sinha, E. B. Sirota, S. Garoff, and H. B. Stanley, Physical Review B **38**, 2297 (1988).
34. D. R. Lee, S. K. Sinha, C. S. Nelson, J. C. Lang, C. T. Venkataraman, G. Srajer, and R. M. Osgood, Physical Review B **68**, 224410 (2003).
35. H. A. Durr, E. Dudzik, S. S. Dhesi, J. B. Goedkoop, G. van der Laan, M. Belakhovsky, C. Mocuta, A. Marty, and Y. Samson, Science **284**, 2166 (1999).
36. Z. Q. Qiu, and S. D. Bader, Review of Scientific Instruments **71**, 1243 (2000).
37. K. S. Lee, S. K. Kim, and J. B. Kortright, Applied Physics Letters **83**, 3764 (2003).
38. K. S. Lee, D. E. Jeong, S. K. Kim, and J. B. Kortright, Journal of Applied Physics **97**, 083519 (2005).
39. H. L. Meyerheim, J. M. Tonnerre, L. Sandratskii, H. C. N. Tolentino, M. Przybylski, Y. Gabi, F. Yildiz, X. L. Fu, E. Bontempi, S. Grenier, and J. Kirschner, Physical Review Letters **103**, 267202 (2009).
40. O. Hellwig, J. B. Kortright, K. Takano, and E. E. Fullerton, Physical Review B **62**, 11694 (2000).
41. C. Kao, J. B. Hastings, E. D. Johnson, D. P. Siddons, G. C. Smith, and G. A. Prinz, Physical Review Letters **65**, 373 (1990).
42. J. M. Tonnerre, L. Seve, D. Raoux, G. Soullie, B. Rodmacq, and P. Wolfers, Physical Review Letters **75**, 740 (1995).
43. J. F. MacKay, C. Teichert, D. E. Savage, and M. G. Lagally, Physical Review Letters **77**, 3925 (1996).
44. Y. U. Idzerda, V. Chakarian, and J. W. Freeland, Physical Review Letters **82**, 1562 (1999).
45. K. Starke, F. Heigl, A. Vollmer, M. Weiss, G. Reichardt, and G. Kaindl, Physical Review Letters **86**, 3415 (2001).
46. M. Sacchi, A. Mirone, C. F. Hague, P. Castrucci, R. Gunnella, and M. De Crescenzi, Physical Review B **64**, 012403 (2001).
47. R. M. Osgood, S. K. Sinha, J. W. Freeland, Y. U. Idzerda, and S. D. Bader, Journal of Magnetism and Magnetic Materials **199**, 698 (1999).
48. J. B. Kortright, O. Hellwig, K. Chesnel, S. H. Sun, and E. E. Fullerton, Physical Review B **71**, 012402 (2005).
49. A. Moser, K. Takano, D. T. Margulies, M. Albrecht, Y. Sonobe, Y. Ikeda, S. H. Sun, and E. E. Fullerton, Journal of Physics D-Applied Physics **35**, R157 (2002).

50. M. S. Pierce, R. G. Moore, L. B. Sorensen, S. D. Kevan, O. Hellwig, E. E. Fullerton, and J. B. Kortright, Physical Review Letters **90**, 175502 (2003).
51. M. S. Pierce, C. R. Buechler, L. B. Sorensen, J. J. Turner, S. D. Kevan, E. A. Jagla, J. M. Deutsch, T. Mai, O. Narayan, J. E. Davies, K. Liu, J. H. Dunn, K. M. Chesnel, J. B. Kortright, O. Hellwig, and E. E. Fullerton, Physical Review Letters **94**, 017202 (2005).
52. M. S. Pierce, C. R. Buechler, L. B. Sorensen, S. D. Kevan, E. A. Jagla, J. M. Deutsch, T. Mai, O. Narayan, J. E. Davies, K. Liu, G. T. Zimanyi, H. G. Katzgraber, O. Hellwig, E. E. Fullerton, P. Fischer, and J. B. Kortright, Physical Review B **75**, 144406 (2007).
53. O. Hellwig, T. L. Kirk, J. B. Kortright, A. Berger, and E. E. Fullerton, Nature Materials **2**, 112 (2003).
54. O. Hellwig, A. Berger, J. B. Kortright, and E. E. Fullerton, Journal of Magnetism and Magnetic Materials **319**, 13 (2007).
55. S. Eisebitt, J. Luning, W. F. Schlotter, M. Lorgen, O. Hellwig, W. Eberhardt, and J. Stohr, Nature **432**, 885 (2004).
56. A. Tripathi, J. Mohanty, S. H. Dietze, O. G. Shpyrko, E. Shipton, E. E. Fullerton, S. S. Kim, and I. McNulty, Proceedings of the National Academy of Sciences of the United States of America **108**, 13393 (2011).
57. C. Gutt, S. Streit-Nierobisch, L. M. Stadler, B. Pfau, C. M. Gunther, R. Konnecke, R. Fromter, A. Kobs, D. Stickler, H. P. Oepen, R. R. Faustlin, R. Treusch, J. Feldhaus, E. Weckert, I. A. Vartanyants, M. Grunze, A. Rosenhahn, T. Wilhein, S. Eisebitt, and G. Grubel, Physical Review B **81**, 4 (2010).
58. J. M. Tonnerre, E. Jal, E. Bontempi, N. Jaouen, M. Elzo, S. Grenier, H. L. Meyerheim, and M. Przybylski, European Physical Journal-Special Topics **208**, 177 (2012).
59. L. G. Parratt, Physical Review **95**, 359 (1954).
60. H. C. Mertins, F. Schafers, X. Le Cann, A. Gaupp, and W. Gudat, Physical Review B **61**, R874 (2000).
61. D. Rudolf, C. La-O-Vorakiat, M. Battiato, R. Adam, J. M. Shaw, E. Turgut, P. Maldonado, S. Mathias, P. Grychtol, H. T. Nembach, T. J. Silva, M. Aeschlimann, H. C. Kapteyn, M. M. Murnane, C. M. Schneider, and P. M. Oppeneer, Nature Communications **3**, 6 (2012).
62. S. Valencia, A. Gaupp, W. Gudat, L. Abad, L. Balcells, and B. Martinez, Applied Physics Letters **90**, 252509 (2007).
63. S. Valencia, A. Gaupp, W. Gudat, L. Abad, L. Balcells, and B. Martinez, Journal of Applied Physics **104**, 023903 (2008).
64. J. B. Kortright, S. K. Kim, E. E. Fullerton, J. S. Jiang, and S. D. Bader, Nuclear Instruments & Methods A **467**, 1396 (2001).
65. M. Pretorius, J. Friedrich, A. Ranck, M. Schroeder, J. Voss, V. Wedemeier, D. Spanke, D. Knabben, I. Rozhko, H. Ohldag, F. U. Hillebrecht, and E. Kisker, Physical Review B **55**, 14133 (1997).
66. K. S. Lee, S. K. Kim, and J. B. Kortright, Journal of Applied Physics **96**, 7414 (2004).
67. C. La-O-Vorakiat, E. Turgut, C. A. Teale, H. C. Kapteyn, M. M. Murnane, S. Mathias, M. Aeschlimann, C. M. Schneider, J. M. Shaw, H. T. Nembach, and T. J. Silva, Physical Review X **2**, 011005 (2012).
68. S. Mathias, C. La-O-Vorakiat, P. Grychtol, P. Granitzka, E. Turgut, J. M. Shaw, R. Adam, H. T. Nembach, M. E. Siemens, S. Eich, C. M. Schneider, T. J. Silva, M. Aeschlimann, M. M. Murnane, and H. C. Kapteyn, Proceedings of the National Academy of Sciences of the United States of America **109**, 4792 (2012).
69. C. La-O-Vorakiat, M. Siemens, M. M. Murnane, H. C. Kapteyn, S. Mathias, M. Aeschlimann, P. Grychtol, R. Adam, C. M. Schneider, J. M. Shaw, H. Nembach, and T. J. Silva, Physical Review Letters **103**, 257402 (2009).
70. S. M. Valvidares, M. Huijben, P. Yu, R. Ramesh, and J. B. Kortright, Physical Review B **82**, 235410 (2010).
71. K. H. Stone, S. M. Valvidares, and J. B. Kortright, Physical Review B **86**, 024102 (2012).
72. J. Goulon, C. Goulon-Ginet, A. Rogalev, V. Gotte, C. Malgrange, C. Brouder, and C. R. Natoli, Journal of Chemical Physics **108**, 6394 (1998).
73. J. Goulon, A. Rogalev, C. Goulon-Ginet, G. Benayoun, L. Paolasini, C. Brouder, C. Malgrange, and P. A. Metcalf, Physical Review Letters **85**, 4385 (2000).
74. J. Goulon, A. Rogalev, F. Wilhelm, C. Goulon-Ginet, P. Carra, D. Cabaret, and C. Brouder, Physical Review Letters **88**, 237401 (2002).
75. P. Carra, A. Jerez, and I. Marri, Physical Review B **67**, 045111 (2003).
76. J. Goulon, A. Rogalev, F. Wilhelm, N. Jaouen, C. Goulon-Ginet, P. Carra, I. Marri, and C. Brouder, Physica Scripta **T115**, 54 (2005).

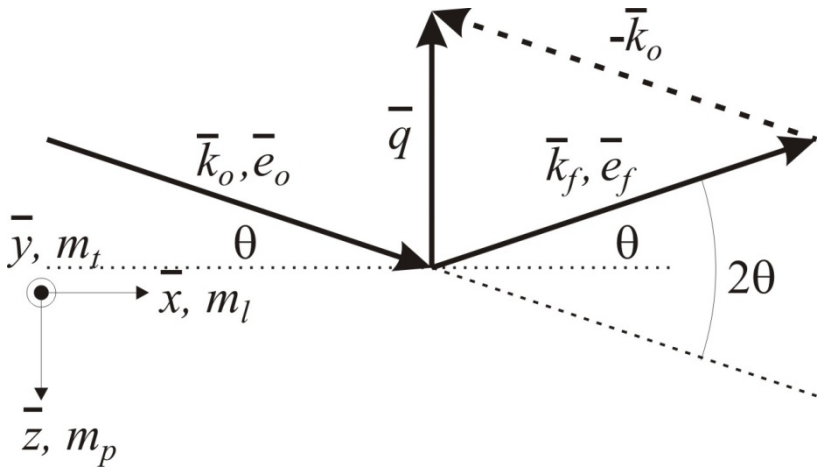

Figure 1. A generalized scattering diagram in which the difference of incident and scattered wavevectors defines the scattering vector $\bar{q} = \bar{k}_f - \bar{k}_o$ and scattering plane. The incident and scattered polarization vectors $\hat{e}_{o,f}$ are typically described in terms of orthogonal linear components in (*p)* and perpendicular to (*s*) the scattering plane. The atomic magnetization vector $\hat{m}$ can in general have longitudinal (m_l), transverse (m_t) and polar (m_p) components. The $\hat{m}$ components are defined such that m_l and m_p are in the scattering plane perpendicular and parallel to $\bar{q}$, respectively, and m_t is out of the scattering plane. This 2-dimensional scattering plane is often a good approximation when scanning an aperture detector about an axis. When using a 2-dimensional detector one must consider the appropriate range of scattering planes, vectors, and moment projections.

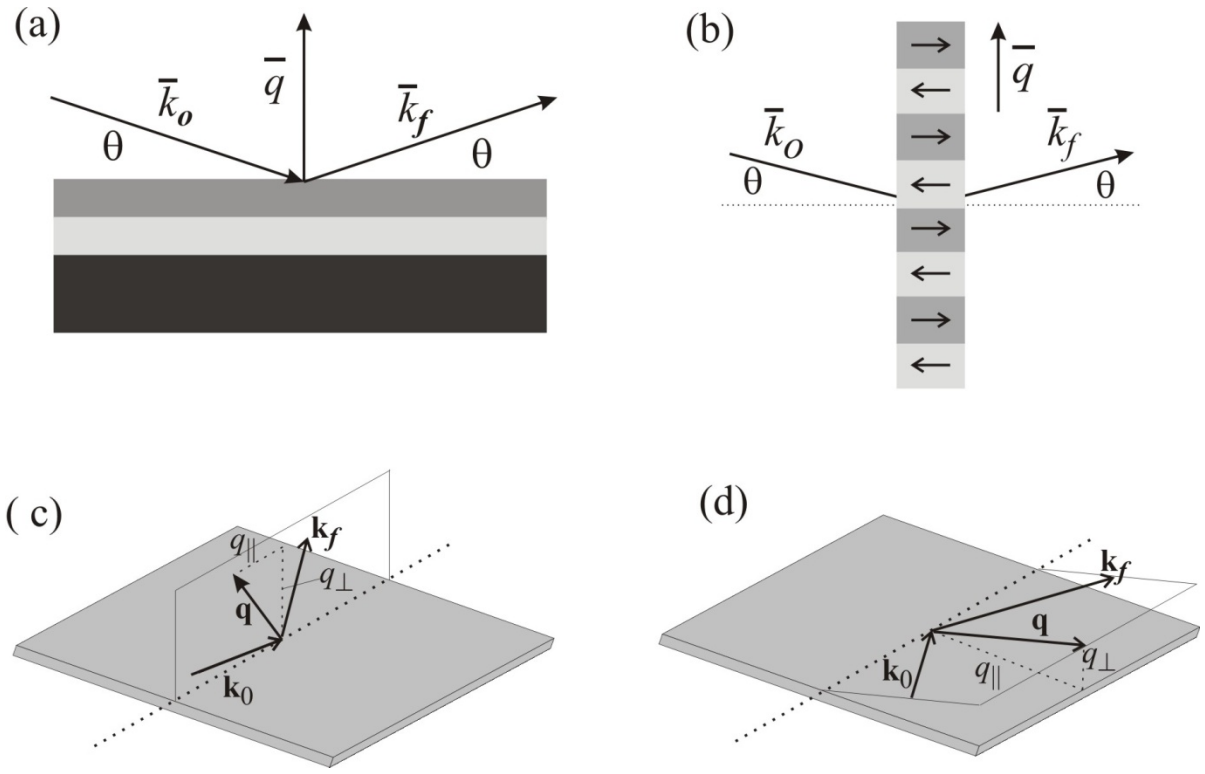

Figure 2. Common scattering geometries and the associated wave- and scattering-vectors. Specular reflection (a) and symmetric transmission (b) geometries position the $\bar{q}$ along the surface normal and in the film plane and optimize coupling to in-depth, and in-plane structure, respectively. Off-specular reflectance (c) and grazing incidence (d) geometries provide both in-plane and out-of-plane $\bar{q}$ components. In general scattered intensities can measure intensity using a point detector corresponding to a small volume of $\bar{q}$-space, or via 2D detectors sampling a larger range of $\bar{q}$-space for a fixed $\bar{k}_o$.

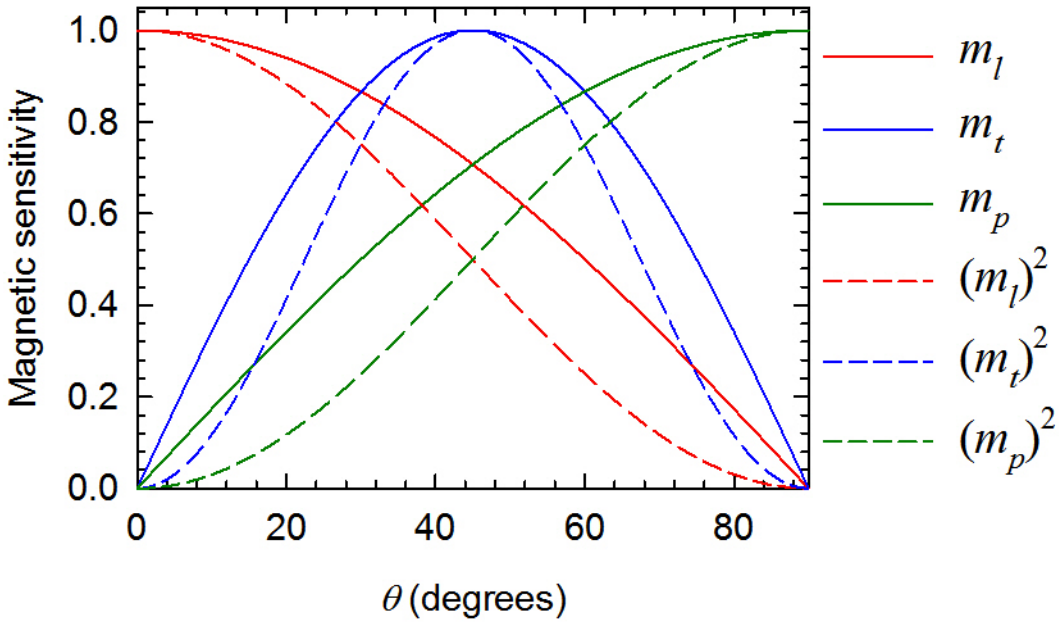

Figure 3. Sensitivity of magnetic scattering to the longitudinal (red), transverse (blue), and polar (green) magnetization components as a function of scattering angle. Solid lines correspond to charge-magnetic intensity terms while dashed lines correspond to pure-magnetic terms.

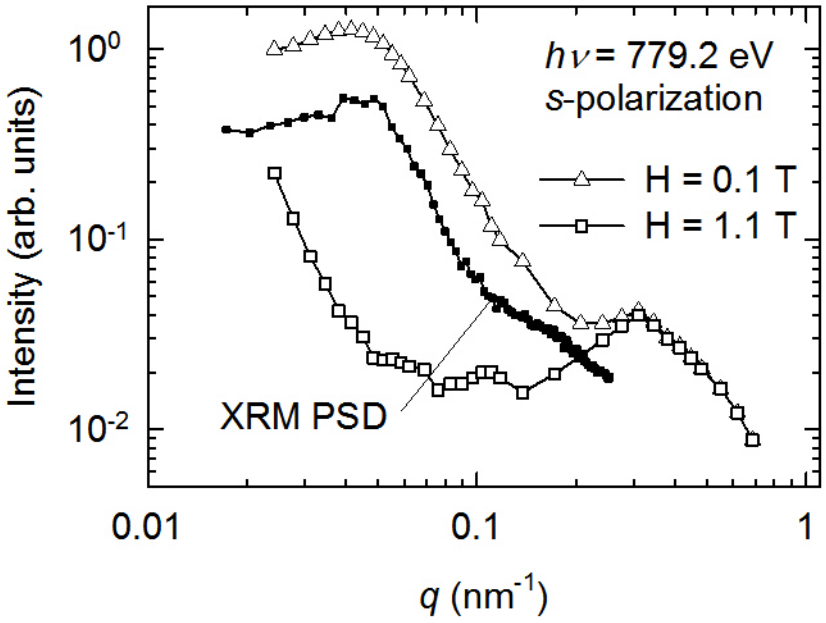

Figure 4. Resonant scattering versus in-plane spatial frequency q near the Co L_3 peak measured a transmission scattering geometry from a Co/Pt multilayer having strong perpendicular anisotropy. Open symbols are intensity measured near remanence (triangles) and saturation (squares). Filled symbols are scaled measurements of the power spectral density (PSD) of magnetic domains from an x-ray microscope image. (After Ref. 22)

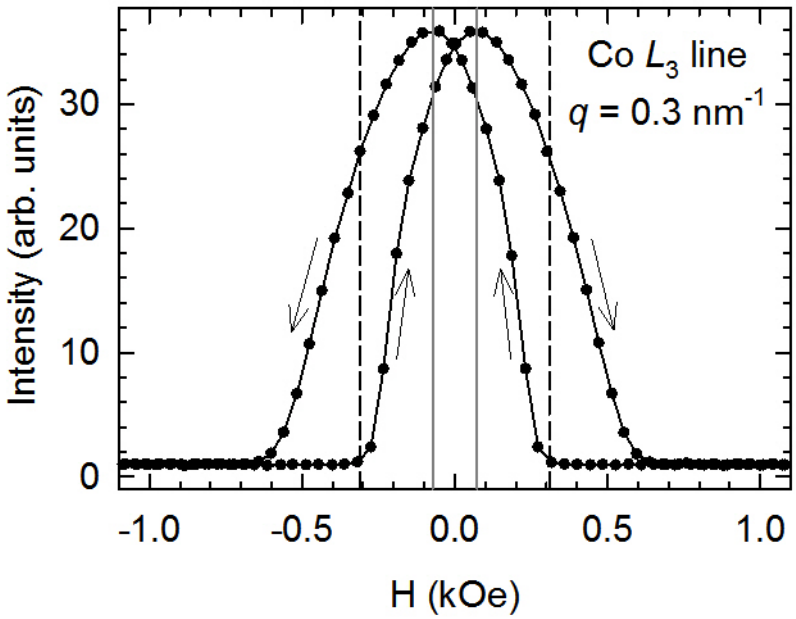

Figure 5. Scattering hysteresis loop from a Co/Pt multilayer at the low-q magnetic domain peak exhibits low intensity when domains are absent, onset of scattering at the domain nucleation field H_N (dashed vertical lines) and saturation of scattering at the coercive field H_C (solid vertical lines). The symmetry of the scattered intensity loop is consistent with its origin in pure-magnetic scattering. (After Ref. 22)

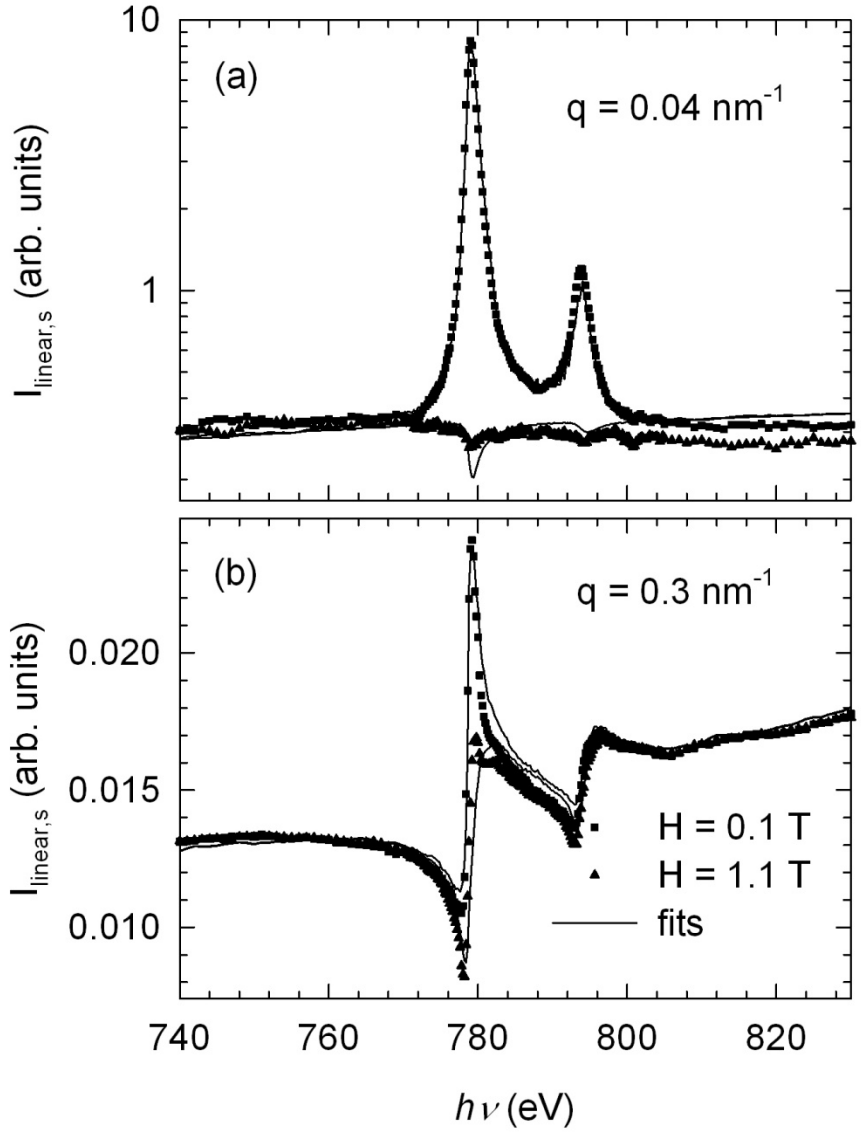

Figure 6. Resonant scattering energy spectra measured using linear incident polarization at spatial frequency q corresponding to the magnetic domain (a) and the polycrystalline grain (b) peak from figure 4. In each panel symbols are data measured near remanence (squares) and saturation triangles), and lines are model fits to the data as described in the text.

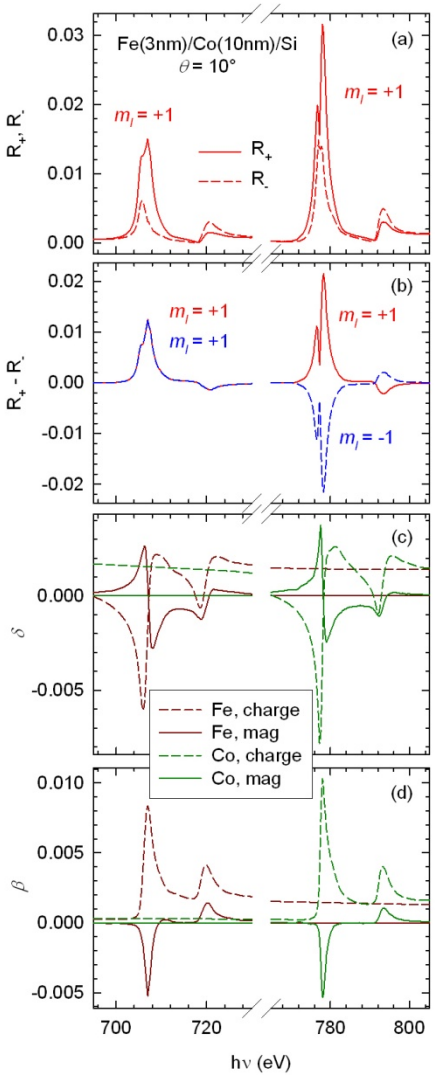

Figure 7. (c) and (d) show the refractive and absorptive spectra, respectively, of the charge and magnetic optical constants for Fe and Co across their L_3 and L_2 edges, and are taken from Refs. 9 and 22. (a) shows calculated reflectance for opposite helicity incident at $\theta = 10°$ on the indicated magnetic heterostructures with Fe and Co longitudinal moments aligned parallel. (b) shows the reflectance difference for both parallel and antiparallel alignment of moments in the adjacent layers. $R_+ - R_-$ changes sign as the Co moment reverses, indicating that this quantity is odd in m_l and hence has predominant charge-magnetic interference.

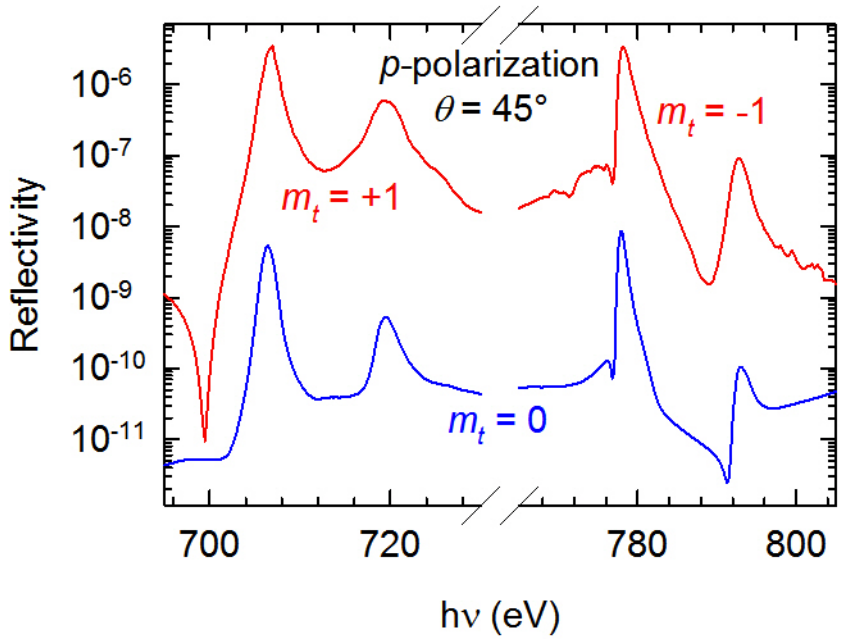

Figure 9. Reflectivity spectra using linear *p*-polarization at $\theta = 45°$ and assuming entirely transverse magnetization in both layers of the Fe/Co bilayer. For red curve the moments in Fe and Co layers are saturated in opposite directions. For the blue curve $m_t = 0$ for both layers, revealing the weak charge-charge scattering at the Brewster angle. The most significant magnetic *intensity* signals using linear polarization are for *p*-polarization and transverse moment changes. These transverse effects have pure-magnetic character.